

Spent Fuel Cask Basket Structure Evaluation with Fast Neutron Imaging*

Haitang Wang[†]

Nuclear Engineering Program, University of Florida, Gainesville FL 32611

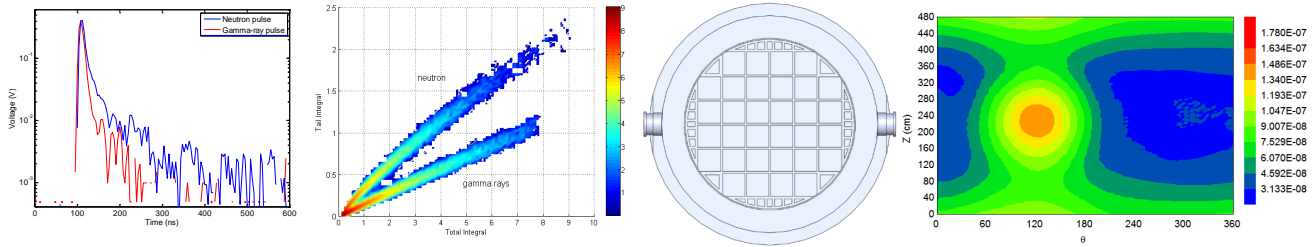


Figure 1: Neutron pulse processing and distribution. (a) demonstrates the individual pulses of a gamma ray and neutron, (b) shows pulse shape discrimination, (c) displays a top view of the cask, and (d) shows the neutron distribution of the neutrons in the air based on an outer point source.

Abstract

Due to the recent development of digital technique involving fast analysis and high recording speed, fast neutrons can be detected through elastic scattering, bringing new opportunities in research and applications because of their short wavelength and large penetration length. In this paper, fission neutrons with energy in the order of MeV will be generated with radioactive sources through Monte Carlo N-Particle platform. Emitted neutrons travel through the wall of a fuel cask after scattering and their travel paths are recorded with Monte Carlo simulations. Those neutrons are selected through a collimator. The selected neutrons are further captured by deployed detectors. The captured signals of those detectors giving the distribution of irradiation according to the fast neutron density. With the algebraic reconstruction technique, the inside view of the cask structure will be shown to evaluate the structure of the cask condition. It would be essential in radiation protection since the spent fuel can last many more years after storage while the cask has a limited lifespan.

Keywords: fast neutrons, Monte Carlo simulation, imaging, time-of-flights

1 Introduction

Neutrons have been an indispensable tool in broad areas like physical, chemical, biological sciences, as well as in material technology and nuclear medicine. They are ideal for the study of the existence of light materials due to elastic collisions, particularly hydrogen. However, unlike thermal neutrons that create charged products such as protons, alpha particles, can be detected efficiently through absorptions, the detection of fast neutrons without moderation has been a challenge. NASA has released a study of the sub-surface hydrogen concentration by detecting background neutrons [Mitrofanov et al. 2002]. The study shows deficits of high-energy neutrons in the southern highlands and northern lowlands of Mars. These deficits suggests that the hydrogen is concentrated in the sub-surface of these areas, as a favorable proof of the existence of ice [Feldman et al. 2002]. However, in their measurements, fast neutrons were moderated by polyethylene before being detected with

³He detectors. The moderated neutrons lack of intrinsic energy information and the scattering of fast neutrons in the moderation materials changes the original spatial locations.

Previously, Jonathan et al. have applied fast neutrons in imaging the core of a Training, Research, Isotopes, General Atomics (TRIGA) test reactor, which gives an evaluation of fast neutron distribution among the reactor core [Beaumont et al. 2015]. However, a reactor with measurements is not practical to most researchers. In this case, we simulate the transports of fast neutrons in a Monte Carlo N-Particle software (MCNP), which is used primarily for the simulation of nuclear processes and particle interactions involving neutrons, photons, and electrons [Pelowitz]. Since fast neutrons travel towards random angles, different detectors are deployed around the cask surface to measure the neutron intensity. Considering the noise due to the count contribution from adjacent source, collimators are associated with the detectors. Those measurements are the projections of the cask at different angle. The back projection algorithm will be applied in image reconstructions, which is the reverse Radon transform [Avinash and Slaney 1998].

2 Overview

2.1 MCNP platform

MCNP is a general-purpose, continuous-energy, generalized-geometry, time-dependent, Monte Carlo radiation-transport code designed to track particle types over broad ranges of energies. For instance, the code deals with transport of neutrons, gamma rays, and coupled transport, i.e., transport of secondary gamma rays resulting from neutron interaction. The MCNP code can also treat the transport of electrons, both primary source electrons and secondary electrons created in gamma-ray interactions. The neutron energy regime is from 10^{-11} MeV to 20 MeV for all isotopes and up to 150 MeV for some isotopes, the photon energy regime is from 1 keV to 100 GeV, and the electron energy regime is from 1 keV to 1 GeV.

2.1.1 Neutron interactions

Even though detailed physics treatment includes coherent scattering and accounts for fluorescent photons after photoelectric absorption, in this study, we mainly focus on the neutron interactions. Neutron interactions with matter can be either scattering or absorp-

[†]e-mail:haitangwang@ufl.edu

*This is unpublished work. Please contact with the author(s) for the redistribution of this paper.

tion reactions. Scattering can result in a change in energy and direction of motion of a neutron but cannot directly cause the disappearance of a free neutron. While absorption leads to the disappearance of free neutrons as a result of a neutron reaction with fission or the formation of a new nucleus and another particle or particles such as protons, alpha particles and gamma rays.

The probability of occurrence of these reactions is primarily dependent on the energy of the neutrons and the properties of the matter with which it is interacting. Materials are mainly differentiated by atomic number and density. We here consider materials that are defined in structure components of the fuel cask, major shielding materials like concrete, and geometries and locations of those materials. The interaction probabilities follow the distribution of cross sections. For fast neutrons, elastic scattering dominates the interaction process. A neutron deposits part of its energy in the materials. However, with moderation, if the energy of the neutron is low enough, neutron absorption is considered, during which a secondary neutrons, secondary gamma rays and other fission products may be released leading to further interactions. Additionally, since an absolute stationary atom does not exists, a collision between the atom and a neutron is affected by the thermal motion of the atom. MCNP uses a thermal treatment based on the free gas approximation to account for the thermal motion. More thorough information is available [Team].

2.1.2 Monte Carlo method

The Monte Carlo methods is very different from deterministic transport methods. Deterministic methods are given by analytical models which consider all interaction scenarios. For instance, the transport of fast neutrons, the transfer of energy, and light productions are described based on the Peierls-formula convoluted with the material light output function from measurements [Wang and Enqvist 2015]. However, it is impossible to expand the analytical model into high order collision due to prohibitive computational time. On the contrary, the Monte Carlo method obtains answers by simulating individual particles and recording some aspects of their average behavior. The individual distributions governing these events are statistically sampled to describe the total phenomenon.

2.2 Emission computed tomography

Emission computed tomography is a type of tomography involving radioactive emission, including Position Emission Tomography (PET) and Single-photon Emission Computed Tomography (SPECT) [Long and Smith 2001]. By detecting the high energy photons and solving the inverse problem that arises, on can measure in vivo the spatial concentration of the radio-pharmaceutical, obtaining insight of the metabolic and physiological processes [Taylor et al. 2014]. Rather than using gamma rays, we detect the distribution fast neutrons which are given by emission sources like spent fuels and Cf-252.

3 MCNP model implementation

3.1 Cask geometry

The cask is composed of a cask body, shell and lid. The inner radius of the cask body is 87.31 cm, the thickness of a containment vessel is 3.81 cm, and the polypropylene disk radius is 89.54 cm. A top view of the cask is shown in Fig.1(c). Meanwhile, the cask body is composed of cask bottom, interior bottom disk and basket. Those diameters are listed in Table 1. For comparison, the geometry of a TN-68 cask can be find in [Shultis 2000]. Certainly, in simulation, we only consider the most significant components,

Table 1: Radial and vertical dimensions of a cask components.

		Component Parameter	Dimensions (cm)
Radial	Body	Cask body inner radius	87.31
		Containment vessel thickness	3.81
		Multilayer steel body	20.32
	Shell	Neutron shield thickness	11.43
		Outer shell thickness	1.27
	Σ	Cask outer radius	124.14
	Lid	Inner shield plate radius	88.27
Outer shield plate/steel lid radius		100.97	
Polypropylene disk radius		89.54	
Vertical	Body	Cask bottom	22.23
		Cask interior bottom disk thickness	3.81
		Basket height	410.85
		Lid-basket gap thickness	3.81
	Lid	Inner shield plate thickness	15.24
		Outer shield plate thickness	11.43
		Polypropylene disk thickness	11.43
	Σ	Total height of cask	478.80
	Shell	Distance from base of cask	31.75
Length		392.43	

while some small parts like nuts and bolts within the structure are neglected, considering these components have very limited impacts on particle transportation.

3.2 Material definition

Most cask components are made of carbon steel, with exceptions of the radial neutron shield, the basket, the top neutron lid, and the cask cavity. The cavity is filled with helium at a pressure of two atmospheres. The out space surrounding the cask is air, which is composed of carbon, nitrogen, oxygen, argon atoms. Additionally, the concrete is a complex mixture of hydrogen, oxygen, sodium, magnesium, aluminum, silicon, potassium, calcium, and iron. Meanwhile, the ground under the cask is natural soil, as seen in Table 2. With the parameters and materials defined for the cask, the model is shown in Fig. 2. It includes soil, polypropylene, helium, concrete, steel, resin, aluminum, and air.

3.3 MCNP input file

3.3.1 Surface and boundary

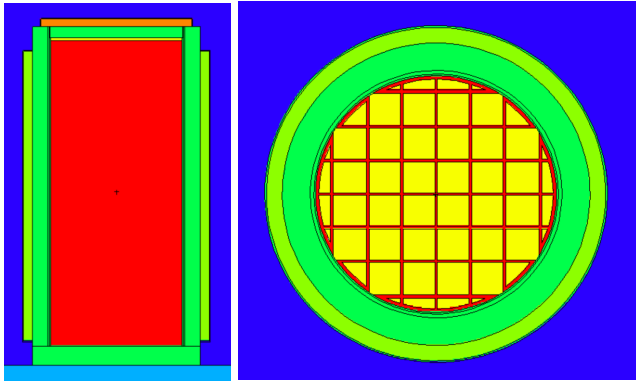
We have defined four types of planes in the model,including x-planes, y-planes, z-planes, and z-cylinders. Additionally, the radial boundary of the universe is set at 1 meter beyond the cask wall. The top boundary is 1 meter above the top of the cask, while the bottom 1 meter into the soil below the concrete pad.

3.3.2 Source definition and position

For the final implementation of the simulation, the cask will have to be loaded with spent fuel using detailed isotopes and fuel burn up calculation. Currently, we have a spontaneous fission source, which is a radioactive source adjusted to emit fast neutrons with energy distribution following the Watt Fission Spectrum statistics. In order to evaluate the neutron transmission inside and outside the cask, and effects of structure materials, the testings are simulated for two runs with the point source near the center of the cask (-12 cm, 12 cm, 231 cm), hereafter referred as the inner point source, and the other point source near the cask wall (-37 cm, 62 cm, 231 cm), respectively.

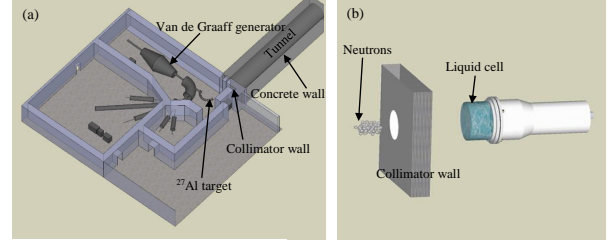
Table 2. Materials definitions

Material	Element/Isotope	Atom/Wt. Fraction
Air (Dry)	$\rho = 0.0012 \text{ g/cm}^3$	
	Carbon	-0.00014
	Nitrogen-14	-0.75519
	Oxygen-16	-0.23179
	Argon	-0.01288
Aluminum	$\rho = 2.72 \text{ g/cm}^3$	
	Aluminum-27	1
Borated Resin	$\rho = 1.687 \text{ g/cm}^3$	
	Hydrogen-1	0.42207
	Boron-10	0.00164
	Boron-11	0.00655
	Carbon-12	0.24658
	Oxygen-16	0.21985
	Aluminum-27	0.10331
Carbon Steel	$\rho = 7.82 \text{ g/cm}^3$	
	Carbon	0.04490
	Iron	0.95510
Concrete	$\rho = 2.32 \text{ g/cm}^3$	
	Hydrogen-1	-0.0056
	Oxygen-16	-0.4983
	Sodium-23	-0.0171
	Magnesium	-0.0024
	Aluminum-27	-0.0456
	Silicon	-0.3158
	Potassium	-0.0012
	Calcium	-0.0192
	Iron	-0.0122
Helium	$\rho = 0.0004 \text{ g/cm}^3$	
	Helium-4	1
Polypropylene	$\rho = 0.90 \text{ g/cm}^3$	
	Hydrogen-1	0.6652
	Carbon-12	0.3348
Soil	$\rho = 1.625 \text{ g/cm}^3$	
	Hydrogen-1	-0.021
	Carbon-12	-0.016
	Oxygen-16	-0.577
	Aluminum-27	-0.050
	Silicon	-0.271
	Potassium	-0.013
	Calcium	-0.041
	Iron	-0.011

**Figure 2:** The geometry of the spent fuel cask. (a) is the section view of the cask model at midplane, and (b) is top view of the cask.

3.3.3 Tallies

Tallies are particularly of interest in determining the feasibility of determining fuel integrity using a neutron field survey: particle transmission, energy spectra shift, and radioactive spatial field

**Figure 3:** Neutron scintillator system testing demonstration. (a) shows a Van de Graaff neutron generator, and (b) shows the setup of a liquid scintillator toward a collimation wall.

shape (signal distortion). Flux tallies are used to return the number of particles that strike a surface per unit area per starting particle. Additionally, the tallies are adjusted according energy cards to sort the score based on their energy level. Tallies are placed inside the basket, the inner radius of the neutron resin, and 1 meter beyond the cask wall. To have a proper simulation, we have set the number of initial particle of 100 million, and requires 40 hours of total core computation time for independent runs.

4 Scintillation detector investigation

Since in realistic measurements, the detection of fast neutron will not capture all the counts by an organic scintillation detector, the resolution of the detector is an important factor affecting the resolution of the image. However, a detector has a different response to fast neutrons with different energy. Thus the investigation of the characteristic response matrix to fast neutrons will be essential to provide further guidance in simulation, as well as the design of collimators.

The detector is 3 inch by 3 inch in diameter and height. The scintillation material is composed of highly purified deuterated benzene, with a D to H ratio of 141:1. The active volume cell is encapsulated in nitrogen environment to minimize the light quenching effect due to oxygen. The wavelength of maximum emission of 425 nm and a time constant of fast decay in the order of nanoseconds [Wang et al. 2016]. The photons are emitted while ionizing particles through the scintillation medium. The scintillation light is further absorbed by a blue-green sensitive bi-alkali photo-cathode. Additionally, the digitizer used is SIS3316 with sampling frequency of 250 MHz. The individual pulses of neutron (in blue) and gamma-ray (in red) from measurements are shown in Fig. 1(a).

Unfortunately, the neutrons unlike gamma rays which can be detected with energy information. The neutron generator provides neutrons with energy up to 10 MeV [Massey et al. 2013]. To have a correct information on the fast neutrons, the detector is arranged 10 meters away to the front surface of the neutron generator, as shown in Fig. 3. The energy of fast neutrons is determined by time-of-flights (TOFs). TOFs are calculated based on the time difference between the system trigger beam and the recorded detector trigger time. More study of the TOF can be found at CEAN [Guerrero et al. 2013].

Meanwhile, as we have noticed that the detector is not only sensitive to fast neutrons, it is also sensitive to gamma rays. Similarly to the approach applied used in Ref. [Beaumont et al. 2015], pulse shape discrimination is used, as shown in Fig.1 (b). In this analysis, total 30 million events are investigated. The higher region is recognized as the fast neutron zone, and the lower region is gamma-ray zone.

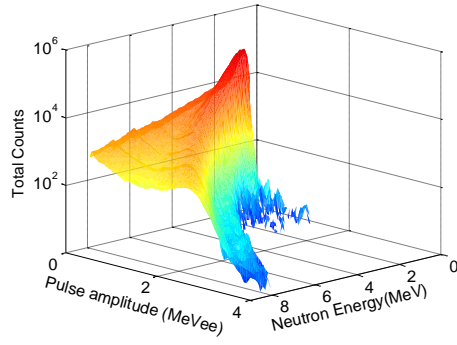


Figure 4: Fast neutron response matrix detected with an organic liquid scintillator.

Combing with the TOFs, the neutron events are organized and the pulse amplitudes are redistributed in histogram. The response matrix is seen in Fig. 4, which plays essential roles in understanding the energy spectrum of neutron sources. More information on the detector resolution is available in [Wang et al. 2016].

5 Results and discussion

Since the geometry of the cask and the materials of all the components have significant impacts on neutron transmission in the cask, tests of the MCNP model have been carried out for two homogeneous neutron point sources. One is placed at the near center and the other is at the near inner radius of the cask body. In order to count the particle numbers at certain location, tallies have been placed at the inside basket, the inner radius of the neutron resin, and 1 meter beyond the cask outside wall. As expected, the neutrons generated by a point source are moderated through scattering. As a result, the energy of the neutrons is shifted with a falling tendency. As Fig. 5 shows, the energy of the initial neutrons follows a distribution of Watt Fission Spectrum. From the near center to the inner basket surface, neutrons traverse through helium gases and aluminum boards. We found that for the case with an inner point source, fast neutrons with energy from 0.1 to 1 MeV dominates the range at the basket inner surface. However, the overall neutron energy distribution of an outer point source is indeed similar to, and the portion of fast neutrons is higher when compared to, that of the case with an inner point source. Even though the refraction of neutrons by the cask body is not quantitatively evaluated, it is important to know part of tally numbers are greater than the neutrons coming from the source directly. The current result of the energy spectra shift because of attenuation does not heavily depend on the position of the source within the cask. However, in a realistic scenario, neutrons that have moderated to thermal neutrons will induce further reactions, including the production of fast neutrons. In our case, we focus more on the transmission of neutrons rather than the complexity of the reaction chains.

Further, neutron fluxes at different locations are plotted on a cylindrical shell. The minimum vertical step length is 10 cm, and the azimuthal angle is 10 degrees along the horizontal axis. Each plot has been normalized. Additional contour smoothing has been performed using the bi-quadratic polynomial technique. Since in field measurements, we will be only able to measure the neutrons outside the cask, the mesh tallies have been applied to both the inside and outside the cask. Neutron distributions at the inner basket and the first cm of air are shown in Figs. 6 and 7. They have revealed that intensities of neutrons in the tallies are ripple-like. Due to the increase of distance from the point source, the neutron intensity decreases along with the vertical axis referring to $z = 231$ cm. As

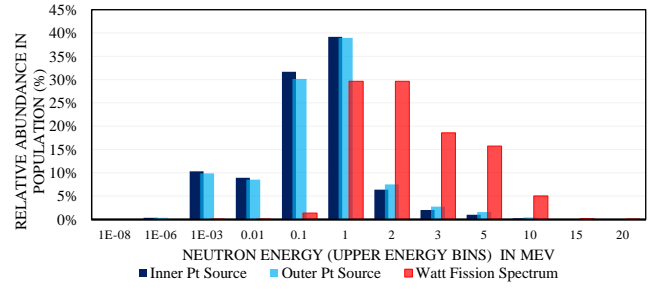


Figure 5: Tally energy at the inner ring of basket for the inner and outer point sources as compared to a Watt Fission Spectrum.

expected, the largest neutron density is found at the azimuthal angle, 120° , where the point source has a shortest distance to the inner basket. Similarly, this phenomenon holds true for the neutron mesh maps at the first 1 cm in the air. This might be hard to process when we have nuclear fuels loaded in the cask, because they intensities are most possibly seen only when the radiation sources are close by. As a result, the count contributions from the sources at or close to the center will be much harder to detect due to impacts from sources at the edge of the cask.

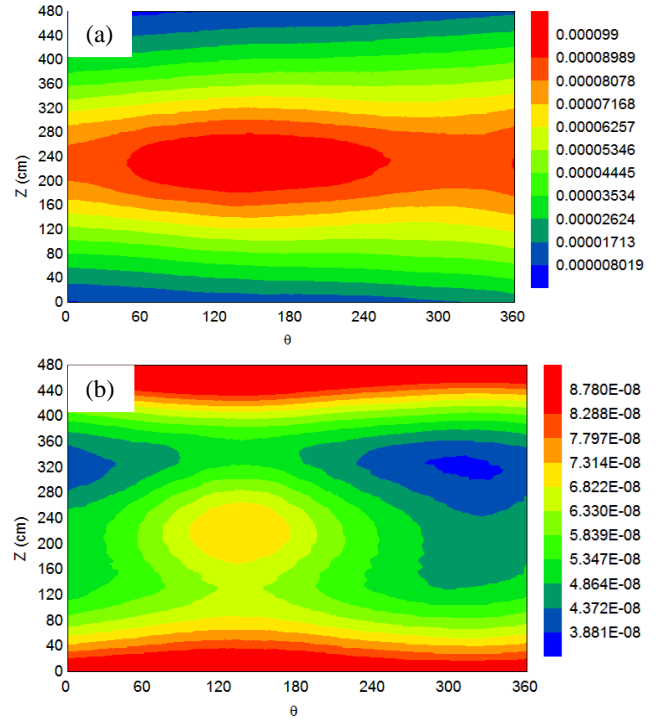


Figure 6: Neutron mapping with the inner point source. (a) the neutron distribution of inner basket ($R = 83.8 - 84.8$ cm); and (b) the neutron distribution of last cm of air ($R = 223.1 - 224.1$ cm).

It is important to note that the neutron has larger intensity at the bottom and the top of cask in the maps than those in the air, as shown in Fig.6(b) and 7(b). This is because neutrons in the air have to penetrate the cask body and the neutron shielding materials. However, the radiation intensity at $z = 0$ or 480 are at the edge of the cask body, and are inside the shielding materials, which means if we expand the range of the Z in investigation, the neutron intensities are expected to decrease to a comparable level to that of the first 1 cm in the air.

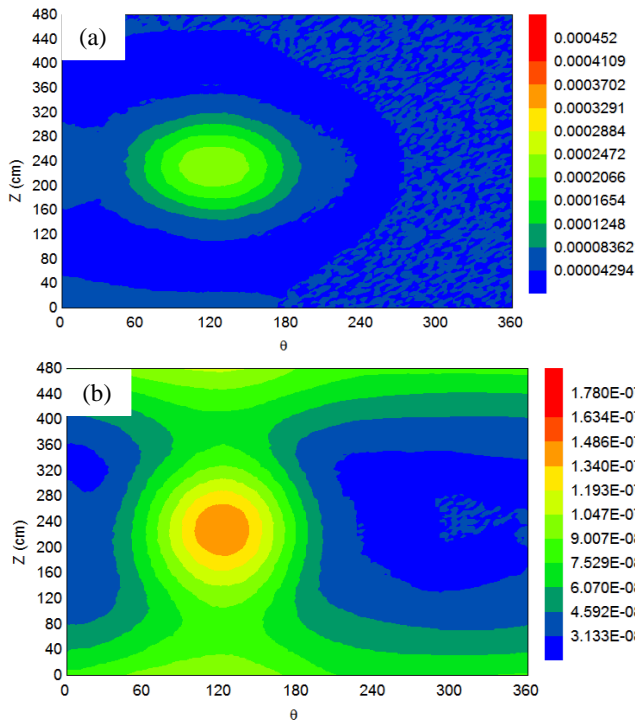


Figure 7: Neutron mapping with the outer point source. (a) the neutron distribution of inner basket ($R = 83.8 - 84.8$ cm); and (b) the neutron distribution of first cm of air beyond the outer cask wall ($R = 223.1 - 224.1$ cm).

Even though, we have the initial mapping results for point neutron sources, the energy distribution of those neutrons recorded in tallies are still unknown, which requires further study. Meanwhile, it's important to aware the high intensity of neutrons does not necessarily mean we will be able to measure those neutrons outside the cask using liquid organic scintillation detectors, as we know that those detectors are most sensitive to the fast neutrons with energy higher than 1 MeV. Current studies are limited to the ability investigation on the fast neutron transmission in the cask. In future, this study will have to be scale up to millions of sources. More through evaluations for the neutron distributions in a 3D space rather than in 2D will be implemented. In this way, a super computer for the computation is necessary, and we plan to move the simulation to HiPerGator.

In addition, we have demonstrated the neutron measurements using a liquid organic scintillator, and have separated neutrons from high gamma-ray background. The understanding of the characteristic response of the detector will provide further guidance in neutron population monitoring and the design of collimators during simulations.

6 Conclusions

In this work, we have built a MCNP model for a spent fuel cask with careful descriptions in the geometry, components and materials. The model has been tested with two independent runs with the setting of two homogeneous neutron sources with energy described in Watt Fission distribution. We found that the overall energy shift of emitted neutrons does not strongly dependent on the position of the neutron sources. However, the neutron meshes show that the relative higher neutron densities have appeared at the tallies closer to the point source. Meanwhile, we have reported the characteristic

response of the detector to fast neutrons. However, the resolution of the detector is not yet applied to simulations. In near future, modifications of the simulation based on the detector characters will be carried out. Meanwhile, the neutrons mesh for the whole cask will also provided in addition to the loading of nuclear fuels.

Acknowledgements

This work is mainly for the CAP6701 project at the University of Florida, and many thanks to Prof. Corey Toler-Franklin for pushing this work forward.

References

- AVINASH, K., AND SLANEY, M. 1998. *Principles of Computerized Tomographic Imaging*. IEEE Press.
- BEAUMONT, J., MELLOR, M., VILLA, M., AND JOYCE, M. 2015. High-intensity power-resolved radiation imaging of an operational nuclear reactor. *Nature Communication* 6, 8592.
- FELDMAN, W., BOYNTON, W., TOKAR, R., PRETTYMAN, T., AND GASNAULT, O. 2002. Global distribution of neutrons from mars: Results from mars odyssey. *Science* 297, 5577 (July), 75–78.
- GUERRERO, C., TSINGANIS, A., BERTHOUMIEUX, E., BARBAGALLO, M., BELLONI, F., GUNSING, F., WEI, C., CHIAVERI, E., CALVIANI, M., AND ET AL. 2013. Performance of the neutron time-of-flight facility neutron tof at cern. *European Physical Journal A* 49, 27–42.
- LONG, N., AND SMITH, C. 2001. Causes and imaging features of false positives and false negatives on 18f-pet/ct in oncologic imaging. *Insights Imaging* 2, 679–689.
- MASSEY, T., AL-QURAISHI, S., BRIENT, C., GUILLEMETTE, J., GRIMES, S., AND JACOBS, D. 2013. A measurement of the $^{27}\text{Al}(\text{d},\text{n})$ spectrum for use in neutron detector calibration. *Nuclear Science and Engineering* 129, 175–179.
- MITROFANOV, I., ANFIMOV, D., KOZYREV, A., LITVAK, M., SANIN, A., TRETYAKOV, V., KRYLOV, A., AND V. SHVETOV, E. A. 2002. Maps of subsurface hydrogen from the high energy neutron detector, mars odyssey. *Science* 297, 5578 (July), 78–81.
- PELOWITZ, D. B. *MCNP User's Manual*. Los Alamos National Laboratory.
- SHULTIS, J. 2000. Radiation analysis of a spent fuel storage cask. Tech. rep., Kansas State University, Department of Mechanical and Nuclear Engineering, 01.
- TAYLOR, B., KIRBY, G., HUGHES, S., CHOWDHURY, S., PAYNE, H., AND CCOOK, G. 2014. Current status of choline-pet and prostate cancer. *Prostate Disease* 5, 34–37.
- TEAM, X.-. M. C. *Monte Carlo N-Particle Transport Code System Including MCNP5-1.60 and MCNPX-2.7.0 and Data Libraries*. Los Alamos National Laboratory, Los Alamos, New Mexico.
- WANG, H., AND ENQVIST, A. 2015. Pulse height model for deuterated scintillation detectors. *Nuclear Instruments and Methods of Physics Research A* 804, 167–174.
- WANG, H., CARTER, D., MASSEY, T., AND ENQVIST, A. 2016. Neutron light output function and resolution investigation of the deuterated organic liquid scintillator ej-315. *Radiation Measurements*, 1–8.